A Novel Flow Reactor for Studying Reactions on Liquid Surfaces Coated by Organic Monolayers: Methods, Validation, and Initial Results

D. A. Knopf,*,†,§ L. M. Cosman,† P. Mousavi,‡ S. Mokamati,‡ and A. K. Bertram†

Department of Chemistry and Department of Mechanical Engineering, University of British Columbia, British Columbia, Canada, and School of Marine and Atmospheric Sciences/Institute for Terrestrial and Planetary Atmospheres, Stony Brook University, New York 11794

Received: July 20, 2007; In Final Form: August 15, 2007

A new flow reactor has been developed that allows the study of heterogeneous kinetics on an aqueous surface coated by an organic monolayer. Computational fluid dynamics simulations have been used to determine the flow characteristics for various experimental conditions. In addition a mathematical framework has been developed to derive the true first-order wall loss rate coefficient, k_w^{1st}, from the experimentally observed wall loss rate, k_{obs}. Validation of the new flow reactor is performed by measuring the uptake of O_3 by canola oil as a function of pressure and flow velocity and the reactive uptake coefficients of N_2O_5 by aqueous 60 wt % and 80 wt % H_2SO_4. Using this new flow reactor, we also determined the reactive uptake coefficient of N_2O_5 on aqueous 80 wt % H_2SO_4 solution coated with an 1-octadecanol ($C_{18}H_{37}OH$) monolayer. The uptake coefficient was determined as $(8.1 \pm 3.2) \times 10^{-4}$, which is about 2 orders of magnitude lower compared to the reactive uptake coefficient on a pure aqueous 80 wt % H_2SO_4 solution. Our measured reactive uptake coefficient can be considered as a lower limit for the reactive uptake coefficient of aqueous aerosols coated with organic monolayers in the atmosphere, because in the atmosphere organic monolayers will likely also consist of surfactants with shorter lengths and branched structures which will have a smaller overall effect.

Introduction

Reactions between aerosol particles and gas-phase species, often termed heterogeneous reactions, have been identified to play a crucial role in the atmosphere. These reactions can lead to significant changes in atmospheric composition.[1−13] For example the hydrolysis of N_2O_5 on and in aqueous H_2SO_4 aerosol particles represents an important heterogeneous reaction acting as a sink for NO_x (NO and NO_2) in the troposphere.[3,12]

A majority of the previous work in the area of heterogeneous atmospheric chemistry has focused on reactions involving aqueous inorganic particles. However, tropospheric particles can consist of a large fraction of organic material (see, e.g., Heintzenberg[14] and Kanakidou et al.[15]) and some of these organic molecules can act as surfactants that may form organic monolayers on the surface of aqueous inorganic particles.[16−27] These organic monolayers may limit the transfer of molecules across the air−aqueous interface and, hence, reduce reaction rates between gas-phase species and the aqueous particles. Recently, researchers have begun to investigate the effect of organic monolayers on heterogeneous chemistry of aqueous aerosol particles.[28−39] Nevertheless, the effect of organic monolayers on atmospheric chemistry still remains unclear.

A possible experimental technique for studying the effect of an organic monolayer on the heterogeneous chemistry of aqueous solutions involves aerosol flow tube reactors where the gas-phase loss to the aerosol particles is measured (see, for example, Hanson and Lovejoy,[40] Fried et al.,[41] Hu and Abbatt,[42] Robinson et al.,[43] Hallquist et al.,[44] Kane et al.,[45] Thornton and Abbatt,[32] and McNeill et al.[35]). However, in this case, determining important properties of the organic monolayers, such as surface tension and packing density, directly on submicron particles is difficult.

Here we have developed a new flow reactor for studying heterogeneous reactions on aqueous solutions coated with organic monolayers. The advantage of this new flow reactor is that it allows us to study heterogeneous reactions using well characterized organic monolayers. For example, we can determine the surface tension and the packing density of the organic monolayer at the air-aqueous interface prior to and after studying the heterogeneous chemistry. This allows us to correlate properties of the organic monolayer with the heterogeneous reaction rates.

In this paper we first describe the new flow reactor and present computational fluid dynamics simulations that are used to characterize the flow dynamics in the reactor. Then we present a mathematical procedure to derive the first-order wall loss rate constant, k_w^{1st}, and the reactive uptake coefficient, γ, from our experimentally observed first-order wall loss rate constant, k_{obs}. (The reactive uptake coefficient is defined as the ratio of the molecules removed from the gas phase by reactions to the total gas-surface collisions.) Next, to validate our new apparatus and mathematical procedure for data analysis, we present measurements of the reactive uptake of N_2O_5 by aqueous H_2SO_4 solutions and measurements of the reactive uptake of O_3 by liquid canola oil. We choose these reactions for validation purposes because they have been studied several times in the past using well developed experimental procedures. Finally, we carry out a preliminary study of the reactive uptake coefficient of N_2O_5 on aqueous H_2SO_4 solutions coated with an insoluble

* To whom correspondence should be addressed. E-mail: Daniel.Knopf@stonybrook.edu.
† Department of Chemistry, University of British Columbia.
‡ Department of Mechanical Engineering, University of British Columbia.
§ Stony Brook University.

10.1021/jp075724c CCC: $37.00
Published on Web 10/11/2007

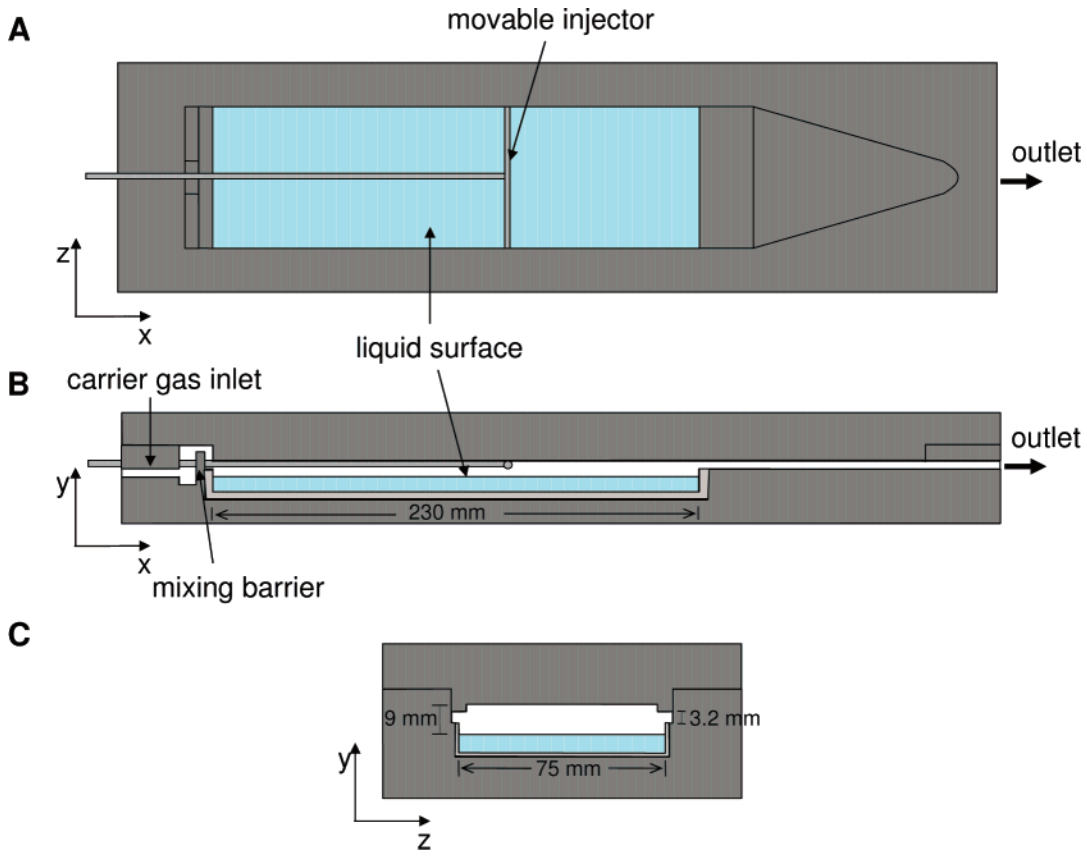

Figure 1. New flow reactor. (A) Top view of the flow reactor without the cover. The main flow is from left to right. The liquid surface in a quartz trough, the movable T-shaped injector, and the corresponding coordinate system are indicated. (B) Side view of the flow reactor including the top cover. The carrier gas inlet, mixing barrier, length of the liquid surface, and corresponding coordinate system are indicated. (C) Cross section of the flow reactor. The width of the liquid surface is given, and the grooves that support the injector are represented.

organic monolayer. We end by discussing the atmospheric implications of the latter results.

Experimental Section

New Flow Reactor. Figure 1 shows a schematic of the newly developed flow reactor. Figure 1A shows a top view with the cover removed, and Figure 1B and 1C show a side view and a front view, respectively. The injector is not included in the front view for clarity. The main body of the reactor is made from aluminum, and it can be temperature controlled by circulating coolant through channels in the aluminum body. Located on the bottom surface of the reactor is a glass trough, which is filled with the aqueous solution, and this aqueous solution can be covered with an organic monolayer. The gas-phase reactant is introduced to the flow reactor by a movable T-shaped injector, which slides just above the liquid surface. The T-shaped injector is equipped with 6 exit holes 0.2 mm in diameter, which point toward the top of the reactor and which distribute the gas-phase reactant evenly across the width of the flow cell. The carrier gas enters the flow reactor through inlets at the back of the flow cell. The gas stream entering the reactor first flows against a barrier to ensure mixing before reaching the liquid surface.

Shown in Figure 1C are the dimensions of the open channel above the liquid surface through which the gases flow. The open channel is close to a perfect rectangular channel geometry, except for the small grooves on the side, which support the movable injector. When designing the flow cell reactor the height of the open channel (distance above the liquid surface in the *y*-direction) was kept as small as possible to reduce the effect of diffusion to the aqueous solution on the overall loss process of the gas-phase reactants. This height was typically less than 10 mm. The width (distance in the *z*-direction) of the open channel was chosen in such a way that the ratio of the height to width, which is also called the aspect ratio (ϵ) is as small as reasonably possible. This simplified the calculations necessary to extract k_w^{1st} and γ from the experimental data (see below). In addition, the length of the flow cell (distance in the *x*-direction) was chosen so that the carrier gas was fully developed over most of the length of the liquid surface (see below).

A chemical ionization mass spectrometer (CIMS) is connected to the outlet of the flow reactor to measure the gas-phase reactant concentration.[46,47] A typical reactive uptake experiment involves measuring the gas-phase reactant concentration as a function of position of the T-shaped injector. By varying the position of the injector, we varied the reaction time between the gas-phase reactant and the liquid surface, and from this data, we determined the observed first-order loss rate, k_{obs}. From k_{obs} we then determined the first-order wall loss rate, k_w^{1st}, and the reactive uptake coefficient, γ, of the trace gas-phase species to the aqueous solution (see below for the procedure to determine k_w^{1st} and γ from k_{obs}). The total pressure in the flow reactor is measured through a 0.64 cm port in the center of the flow reactor cover using a capacitance pressure gauge. Three additional ports, 0.16 cm in diameter, allow the measurement of gas and solution temperature using K-type thermocouples. All aluminum surfaces inside the flow reactor are coated with Halocarbon wax to minimize loss of the gas-phase species to the walls.

Details of the Reactive Uptake Experiments. Three different kinds of reactive uptake experiments have been conducted: First, to validate our apparatus and mathematical procedure for data analysis, we measured the reactive uptake coefficient of

O_3 on liquid canola oil and the reactive uptake coefficient of N_2O_5 on aqueous H_2SO_4 solutions (without organic monolayers). After the validation experiments, we measured the reactive uptake coefficient of N_2O_5 by an aqueous H_2SO_4 solution coated with a monolayer of 1-octadecanol ($C_{18}H_{37}OH$).

For the O_3 uptake experiments, we generated O_3 by passing a flow of O_2 over an ultraviolet source. The generated O_3 was collected and stored in a 5 L bulb. During the O_3 uptake experiments the flow of O_2/O_3 that passed through the movable injector varied between 0.9 and 4.5 cm^3 min^{-1} STP (standard temperature and pressure). The flow of the He carrier gas ranged between 0.14 and 2 L min^{-1} STP. This resulted in Reynolds numbers (*Re*) of 0.3−5, indicating laminar flow conditions. O_3 was detected as O_3^- in the mass spectrometer after its chemical ionization by SF_6^-.[46,48] SF_6^- was generated by passing a trace amount of SF_6 in about 2 L min^{-1} N_2 through a ^{210}Po source.[46] O_3 concentrations used in these reactive uptake measurements ranged from 0.53×10^{11} to 1.4×10^{11} molecules cm^{-3}. The total flow velocities used in these experiments ranged from 70 to 470 cm s^{-1}. Within experimental uncertainty, the reactive uptake coefficient was independent of flow rate.

For the second set of experiments N_2O_5 was generated by reacting NO_2 with an excess amount of O_3 in a separate flow system.[47,49−51] The N_2O_5 resulting from this reaction was passed through a glass vessel containing P_2O_5 to convert any residual HNO_3 into N_2O_5 before N_2O_5 was collected in a glass trap held at 193 K. In the N_2O_5 uptake measurements a saturated flow of N_2O_5 of about 4.6−9 cm^3 min^{-1} STP mixed in a He flow of 36−80 cm^3 min^{-1} STP enters the flow reactor through the movable injector. The flow of the H_2O/He carrier gas varies between 50−780 cm^3 min^{-1} STP. This results in laminar flow conditions ($Re = 0.1-1.6$). The relative humidity of the H_2O/He carrier gas is adjusted to the corresponding relative humidity of the aqueous H_2SO_4 solution, which was determined using the AIM model.[52−54] N_2O_5 was detected as NO_3^- after its chemical ionization by I^-.[48] I^- was generated by passing a trace amount of CH_3I in about 2 L min^{-1} STP N_2 through a ^{210}Po source. N_2O_5 concentrations in experiments employing pure aqueous sulfuric acid solutions ranged between 2×10^{10} to 1×10^{11} molecules cm^{-3}. N_2O_5 concentrations in experiments employing aqueous sulfuric acid solutions coated by an organic monolayer ranged between 8×10^9 to 1×10^{12} molecules cm^{-3}. Because we are using low concentrations of reactants in our experiments, the accumulation of reaction products during the course of our experiments is not a concern. For example, if all the HNO_3 produced from the N_2O_5 hydrolysis remained in the solution, the maximum HNO_3 concentration in the solution after 1 h would be at most (assuming $\gamma = 0.01$) 0.02 wt % with the highest N_2O_5 concentrations. The fact that we do not see any dependence of the reactive uptake coefficient on time (see below) and the reactive uptake coefficient is independent of the N_2O_5 concentrations used, further confirms that accumulation of impurities is not an issue.

The flow velocities used in these experiments ranged from 200 to 500 cm s^{-1}. Within experimental uncertainties, the reactive uptake coefficients were independent of this parameter.

Organic Monolayer Preparation. In the experiments where we measured the reactive uptake of N_2O_5 on aqueous sulfuric acid solutions coated with organic monolayers, two types of methods were used to prepare the organic monolayers. The first consisted of depositing a few droplets of solution of 1-octadecanol dissolved in chloroform on the aqueous H_2SO_4 surface.[55,56] The second method consisted of sprinkling octadecanol crystals on the aqueous H_2SO_4 solution.[57−59] Both methods produced an organic monolayer in contact with solid 1-octadecanol. Sulfuric acid solutions were prepared volumetrically using purified water (resistance > 18.2 MΩ).

TABLE 1: Experimental Conditions under Which Flow Experiments and Corresponding CFD Simulations Were Conducted[a]

experiment	mass flow He, STP cm^3 min^{-1}	mass flow H_2O, STP cm^3 min^{-1}	pressure, Torr	% relative humidity	v_{avg}, m s^{-1}
1	176	10	2.6	0.5	1.4
2	875	17	3.9	0.25	4.5
3	1570	18	5.1	0.2	6.0
4	2708	410	9.1	4.1	6.5
5	2655	17	6.9	0.15	7.6
6	3946	17	8.8	0.12	8.7

[a] All experiments and simulations were performed at 298 K.

Chemicals. Listed below are the chemicals, the corresponding purities, and manufacturer used in our studies: N_2 (99.999%, Praxair), He (99.999%, Praxair), SF_6 (99.995%, Praxair), O_2 (99.993%, Praxair), H_2SO_4 (95−98%, Fisher), CH_3I (99%, Aldrich), NO_2 (99.5%, Matheson), P_2O_5 (97%, Aldrich), canola oil (not determined), 1-octadecanol (99%, Aldrich), chloroform (99.9%, Fisher).

Computational Fluid Dynamics Simulations

Computational fluid dynamics (CFD) simulations have been performed to show that the gas flow over the liquid surface has a well developed laminar flow profile for typical experimental conditions used in our experiments. Fully developed laminar flow conditions simplify the data analysis of our experimental results (see below). In addition we use these simulations to visualize the gas flow profiles in our experiments. Also we use the CFD simulations to show that the flow profile of the gas in our reactor is close to the flow profile that would be established in a perfect rectangular channel.

For the simulations, we choose conditions that were the same as some of the conditions used in the reactive uptake experiments. These conditions are listed in Table 1 and cover the typical range of conditions used in this study as well as typical conditions that we plan to use in future studies of reactive uptake measurements on aqueous solutions coated with organic monolayers.

The simulations were carried out with the software package Fluent.[60] Fluent is capable of modeling fluid flow velocity vectors and temperature and pressure contours.[60] The framework of Fluent is based on the conservation of mass, momentum, and energy. First a three-dimensional computational grid (or mesh) that corresponds to the actual experimental dimensions is constructed. Each cross point of the grid represents a node at which the differential equations that describe the conservation of mass, momentum, and energy are replaced by equivalent finite difference approximations. These algebraic equations are solved numerically to yield the variables of the interest such as flow velocity, pressure, and temperature. Iteration of the overall equations using minimization of the corresponding residuals leads to convergence of the numerical solution.

For these calculations, we focus on the flow dynamics of the gas phase and assume the liquid surface is stationary. The three-dimensional segregated solver for laminar conditions has been applied for these simulations. Discretization was performed using the second-order upwind scheme. Wall and gas temperature were set constant to 298 K. Fluid properties are obtained using ideal gas mixing laws and mass diffusivity was derived using a constant dilution approximation.[60]

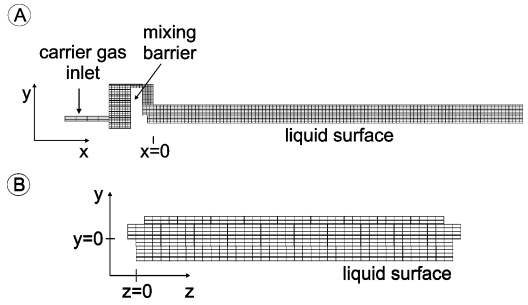

Figure 2. (A) Computational grid that divides the flow reactor volume in hexahedron 3D elements and is used for computational flow dynamic (CFD) simulations. Every cross section indicates a node at which the governing equations describing the flow dynamics are solved. (B) represents the cross section in flow direction.

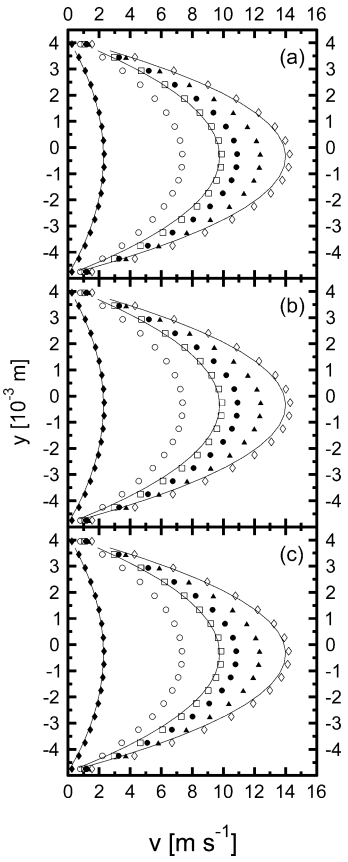

Figure 3. Velocity flow profiles along the *y*-axis derived from CFD simulations for the conditions given in Table 1. (a), (b), and (c) represent the results obtained at $x = 6$, 13, and 20 cm, respectively. Solid diamonds, open circles, open squares, solid circles, solid triangles, and open diamonds represent the flow profiles obtained for conditions 1, 2, 3, 4, 5, and 6 given in Table 1, respectively. Solid lines indicate calculations of the flow profile for a rectangular channel given by Solbrig and Gidaspow.[61]

Figure 2 shows the applied computational grid that divides the open channel above the liquid surface into discrete volumes. Also indicated is the coordinate system used in the calculations. Most computations were performed with a mesh containing 337 984 hexahedron 3D elements. Figure 2B shows a cross sectional view ($y-z$ plane) of the mesh at $x > 0$. This cross section contains 1384 quadrilateral 2D elements. The computational grid shown in Figure 2 resulted in stable numerical solutions. The CFD simulations converged to a numerical solution with residuals smaller than 10^{-6} after 5000 iterations. The convergence criterion given by Fluent is that the normalized

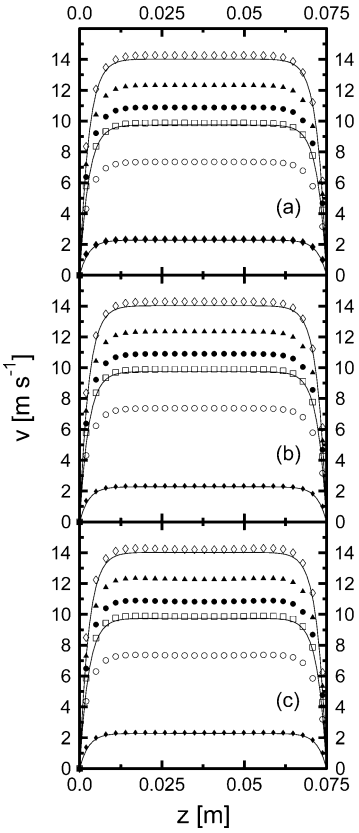

Figure 4. Velocity profiles across the width of the flow reactor (in the *z*-axis) derived from CFD simulations for the conditions given in Table 1. (a), (b), and (c) represent the results obtained at $x = 6$, 13, and 20 cm, respectively. Solid diamonds, open circles, open squares, solid circles, solid triangles, and open diamonds represent the flow profiles obtained for conditions 1, 2, 3, 4, 5, and 6 given in Table 1, respectively. Solid lines indicate calculations of the flow profile for a rectangular channel given by Solbrig and Gidaspow.[61]

unscaled residuals should drop to 10^{-3}.[60] The residuals of all conducted CFD simulations dropped to values 3 orders of magnitude lower than the suggested convergence criterion. For most of our computations we used a total of 5000 iterations. Increasing the iterations up to 20 000 did not change the results significantly.

To ensure that the mesh size was appropriate for our application, we carried out some CFD simulations with a coarser and finer mesh. When the number of mesh elements was decreased by a factor of approximately 6 (coarser mesh: 55724 hexahedron 3D elements), the average velocity, v_{avg}, calculated using the CFD simulations at the exit of the flow reactor, changed by approximately 10% compared to the actual mesh described above. When the number of mesh elements was increased by a factor of approximately 3 (finer mesh: 1129840 hexahedron 3D elements), the calculated v_{avg} only changed by about 2.5%. Because the improvement when going to a finer mesh was considered small, we used the mesh size illustrated in Figure 2 for most of the calculations to reduce the computational time.

Figure 3 shows the flow profiles which develop along the *y*-axis evaluated at $z = 0.0375$ m (i.e., midpoint of the width) The different symbols correspond to the different conditions given in Table 1. Panel a, b, and c of Figure 3 correspond to calculations performed at *x*-axis positions of 6, 13, and 20 cm, respectively. The results indicate a Poiseuille flow along the *y*-axis (i.e., in the vertical direction) between the liquid surface and the top cover of the reactor. The flow profiles do not change

when going from $x = 6$ cm to $x = 20$ cm, indicating a fully developed laminar flow has been established at $x = 6$ cm.

Figure 4 shows the flow profiles that developed across the width of the flow reactor (in the *z*-axis) evaluated at mid-height. Similar to above, the symbols represent the CFD calculations and the different symbols correspond to the different conditions given in Table 1. Panels a, b, and c of Figure 4 were evaluated at *x*-axis positions of 6, 13, and 20 cm. The profile at an *x*-position of 6 cm is the same as the profile at an *x*-position of 20 cm, indicating a fully developed laminar flow at an *x*-position of 6 cm. Figure 4 also indicates that the flow velocity is constant over a majority of the width (*z*-direction).

The flow profiles in our system are very close to the flow profiles one would predict for a rectangular channel with a width equal to 75 mm (which is the width of the liquid surface) and height equal to 9 mm (which is the height of the open channel above the liquid). This is also illustrated in Figures 3 and 4. The solid curves in these figures represent the predicted flow velocities for a rectangular channel with width = 75 mm and height = 9 mm, calculated using the equations presented in Solbrig and Gidaspow.[61] The equations by Solbrig and Gidaspow[61] correspond to fully developed laminar flow. The solid lines are in very good agreement with the predictions from our computational fluid dynamics simulations, which is not surprising because our geometry is very close to the geometry of a rectangular channel.

In Figures 3 and 4 we show that the flows are fully developed after a short distance (<6 cm) in the reactor. Additional CFD analysis (not shown here) indicates that the time to reach a fully developed laminar laminar flow after the mixing barrier is less than 1.5 cm for all the different conditions given in Table 1. This is consistent with the approximate estimates of the time to reach a fully developed flow between two parallel plates with similar dimensions and flow conditions. According to Levich[62] the distance required to reach fully developed flow between two parallel plates can be estimated by

$$l_e \approx 0.1 \cdot a \cdot \mathrm{Re} \tag{1}$$

where *a* is half the height of the flow reactor and *Re* is the Reynolds number. If we use a Reynolds number and height consistent with our experimental conditions we obtain $l_e \approx 0.2$ cm.

The effect of the T-shaped injector on the flow profiles has not been modeled, but it is assumed that the distance to reach a fully developed flow after the T-shaped injector will be similar to the time to reach a fully developed flow at the entrance of the flow reactor. This distance is much less than the length of the reactive surface. For example, for the conditions given in Table 1 the corresponding distances are maximum 5−15 mm. Also this distance will not effect our overall uptake measurements as long as it is relatively short and it remains constant during the uptake measurements. This is discussed in more detail below.

Mathematical Framework To Derive the First-Order Wall Loss Rate Coefficient, k_w^{1st}, and the Reactive Uptake Coefficient, γ

The overall goal of our experiments is to determine the reactive uptake coefficient, γ, of the trace gas-phase species to the aqueous solution, where γ is defined as the fraction of collisions with a surface that result in irreversible loss. As mentioned above, in our experiments we measure the concentration of the trace gas-phase species as a function of injector position. Assuming first-order kinetics, the concentration as a function of position can then be described by the following equation:

$$C(t) = C_0 \exp\left(-\frac{k_{obs} l}{\upsilon_{avg}}\right) \tag{2}$$

where *l* indicates the length of the reactive surface, $C(l)$ is the concentration of the gas-phase reactant at a position *l*, C_0 is the concentration of the gas-phase reactant at $l = 0$, υ_{avg} is the average flow velocity. In our studies we plot the ln [*C*] versus the reaction time given by $t = l/\upsilon_{avg}$ to determine k_{obs}. The position used for the *l* origin (i.e., $l = 0$) is arbitrary because eq 2 shows that k_{obs} can be determined from the relative concentration of *C*.[63] However, it must be fixed at some distance downstream from the T-shaped injector so that the measurements start only after the reactants are well mixed.[63] Typically, we use a value of approximately 2 cm after the T-shaped injector to ensure the reactants are well mixed and the flow is fully developed.

If the heterogeneous reaction at the aqueous surface is slow, then k_{obs} equals the first-order wall loss rate constant (k_w^{1st}), and then γ can be calculated from k_w^{1st} using the following equation, which is also corrected for the non-Maxwellian velocity distribution[64,65]

$$\frac{1}{\gamma} = \frac{cA}{4k_w^{1st}V} + \frac{1}{2} \tag{3}$$

where A = length × width is the reactive surface area and *V* is the gas flow volume above this area. *c* is the thermal molecular speed of the reactant gas species given by $c = \sqrt{8RT/\pi M}$, where *R* is the general gas constant, *T* is the temperature of the gas species, and *M* is the molecular weight of the gas species.

For our analysis, we assume that the reactive uptake coefficient is independent of time, which is supported by experimental results. In a set of separate experiments we first pushed the injector passed the liquid solution (no exposure to the liquid) and the signal of the reactive gas (either N_2O_5 or O_3) is recorded. Then we pull the injector back several centimeters and observe the signal over the period of several minutes. As soon as the injector is pulled back, the signal decreases and then rapidly stabilizes. Over the observation time, the signal is constant. In addition, during the course of O_3 and N_2O_5 uptake experiments we did not observe any changes in the reactive uptake coefficient with time. We performed up to eight uptake experiments on three freshly prepared liquid surfaces, which took 1−3 h. Within this time frame we did not observe any changes of the reactive uptake. The observation that the uptake coefficient was independent of time is consistent with the low reactant concentrations used in our experiments and only a small amount of reactant products accumulating during the course of our experiments as mentioned above.

If the heterogeneous reaction at the aqueous surface is fast, then concentration gradients of the reactive species can develop in the open channel above the liquid surface. In this case, the observed loss rate of the reactive species is controlled by both diffusion to the liquid surface and heterogeneous reaction at the surface, and hence k_{obs} can be significantly less than k_w^{1st}. To determine k_w^{1st} from k_{obs}, gas-phase transport to the reactive surface has to be considered.[63,66−68] Once k_w^{1st} is determined, γ can then be calculated using eq 3.

In the case of a cylindrical flow reactor, an analytical solution exists,[66] which has been implemented into a Fortran program

TABLE 2: Calculated Diffusion Coefficients of N_2O_5 in He, N_2O_5 in H_2O (Vapor), and O_3 in He[69−74]

temp, K	$D_{N_2O_5-He}$, Torr cm^2 s^{-1}	$D_{N_2O_5-H_2O}$, Torr cm^2 s^{-1}	D_{O_3-He}, Torr cm^2 s^{-1}
273	289	72	
295	330	85	
298	336	87	394

code[63] to determine k_w^{1st} from k_{obs}. This solution takes into account concentration gradients of the reactive species that develop in both the axial and radial directions.[63] In other words, this solution takes into account diffusion in the axial and radial directions. For rectangular channel flow reactors with one catalytic wall, an analytical solution exits to determine k_w^{1st} from k_{obs}.[61,67] This analytical solution corrects for concentration gradients that develop in the vertical direction, but it does not correct for concentration gradients that develop in the direction of the bulk flow.[61,67] In most cases this is a very good approximation when fast flows are applied (see below). For completeness, however, we developed a numerical solution to calculate k_w^{1st} from k_{obs}, which corrects for concentration gradients that develop in both the vertical direction and the direction of the bulk flow for arbitrary laminar flow conditions. The numerical method we used to calculate k_w^{1st} from k_{obs} is described in detail in the Appendix. This procedure basically decouples the effect of mass transport to and reaction at the liquid surface.

When calculating k_w^{1st} from k_{obs} using the procedure outlined in the Appendix, the gas-phase diffusion coefficients are needed. The diffusion coefficients applied in this study are calculated using molecular parameters following the procedure outlined previously.[46,69−74] These calculated diffusion coefficients are given in Table 2 as a function of experiment temperature. The binary N_2O_5 diffusion coefficient in the He/H_2O gas mixture for given water partial pressure, p_{H_2O}, and He partial pressure, p_{He}, is then calculated using[75]

$$D_{N_2O_5} = \left(\frac{p_{H_2O}}{D_{N_2O_5-H_2O}} + \frac{p_{He}}{D_{N_2O_5-He}} \right)^{-1} \quad (4)$$

Results and Discussion of Uptake Experiments

Validation of the Flow Cell and the Data Analysis Procedure. As mentioned above, to validate our flow cell and data analysis methodology, we measured the reactive uptake of O_3 on canola oil and N_2O_5 on aqueous uncoated H_2SO_4 solutions. Shown in Figure 5 are examples of typical results. Plotted is the natural logarithm of the gas-phase reactant signal as a function of reaction time (determined from the average flow velocity). Each of the data points represents the gas-phase reactant concentration as a function of injector position. The data for each uptake experiment was fitted by a straight line and the observed first-order loss rate, k_{obs}, was determined from the slope. The example of the uptake of O_3 by canola oil presented in Figure 5 results in $k_{obs} = 7.8$ s^{-1}. The calculated k_w^{1st} value derived from the experimental data and using the procedure outlined in the Appendix is 9.3 s^{-1}. Hence, k_{obs} is corrected by 19%. In the case of the reactive uptake of N_2O_5 by aqueous H_2SO_4 shown in Figure 5 the k_{obs} value is 116.5 s^{-1} and the corresponding k_w^{1st} value is 372 s^{-1}, which is about 318% higher than k_{obs}. These results emphasize the importance of the correction for diffusion.

For the reaction between O_3 and canola oil we carried out two sets of experiments. In the first set, we measured γ for O_3 on canola oil as a function of total pressure while keeping the flow velocity relatively constant (the flow velocity was held between 200 and 300 cm s^{-1}). In the second set of experiments we measured γ for O_3 on canola oil as a function of flow velocity while keeping the total pressure constant (at 3 Torr). Figure 6a shows the results of uptake measurements of O_3 by canola oil as a function of total pressure in the flow reactor. Each data point in the Figure 6 is the result of 3−16 individual uptake experiments. Uncorrected γ values were obtained by using k_{obs} in eq 3 instead of k_w^{1st}. Corrected values were obtained by using k_w^{1st} in eq 3 as discussed above. The dashed line in Figure 6a represents the value reported in the literature determined with a cylindrical flow reactor.[76] The shaded region represents the uncertainty in the number reported in the literature.[76] In all cases our measured γ is consistent with the literature data. Figure 6a indicates that the correction for vertical diffusion and diffusion in flow direction is small in all cases. Figure 6b indicates that the correction for diffusion increases with the total pressure as expected. This is due to slower diffusion of the gas-phase reactants to the reactive surface at higher total pressures.

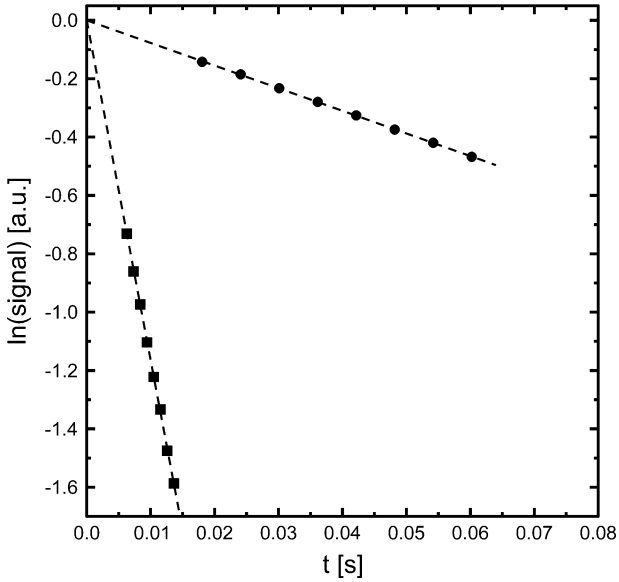

Figure 5. Experimentally derived natural logarithms of the gas-phase signals as a function of reaction time (t). Solid circles and solid squares indicate the uptake of O_3 by canola oil and the uptake of N_2O_5 by aqueous 80 wt % H_2SO_4 solution, respectively. Dashed lines indicate a linear fit to the data.

Figure 7 shows γ values obtained from the uptake of O_3 by canola oil as a function of flow velocity. Also, on the secondary x-axis we have included the Peclet number, which can be interpreted as the ratio between system length and diffusion length (see Appendix). Figure 7a presents uncorrected γ values derived from k_{obs} and corrected values derived from k_w^{1st}. Figure 7 shows that for low flow velocities or Peclet numbers the uncorrected value does not agree with the literature values. Correction for vertical diffusion and diffusion in the direction of the bulk flow is necessary to obtain agreement with the literature data. Figure 7b shows that the correction for diffusion can be large at low flow velocities, as expected. This is due to the increased importance of diffusion in the direction of the bulk flow as the flow velocity is decreased.

As mentioned, for the validation experiments we also studied the uptake of N_2O_5 on aqueous H_2SO_4 solutions (not coated with organic monolayers). At 295 K we studied the uptake on 80 wt % solutions, and at 273 K we studied the uptake on

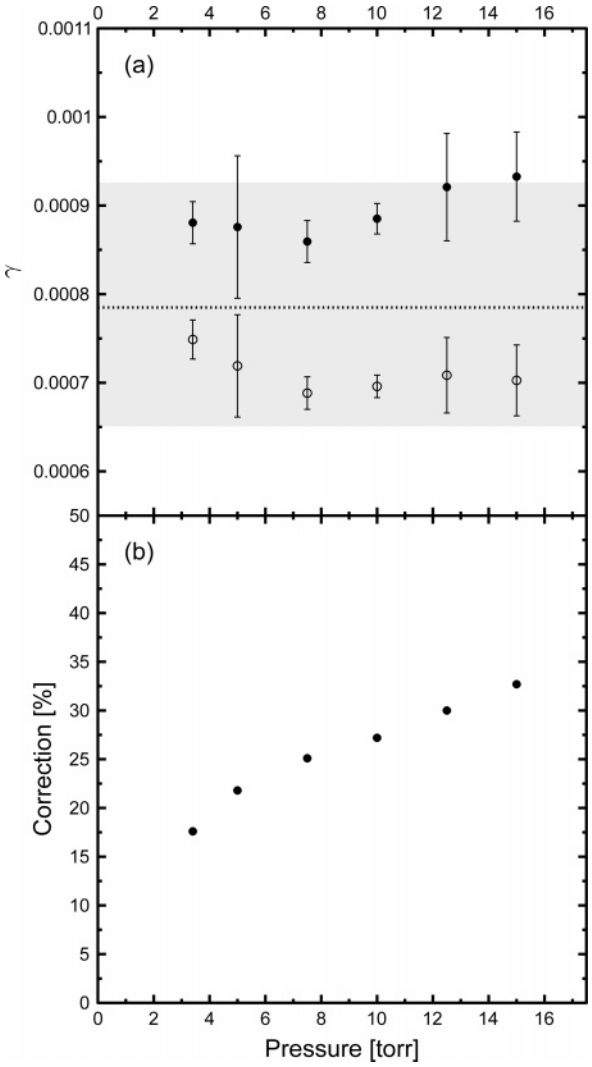

Figure 6. Uptake of O_3 by canola oil as a function of pressure (a). Open circles indicate γ values that have not been corrected for diffusion. Solid circles indicate γ values that have been corrected for vertical diffusion and diffusion in the direction of bulk flow. The dashed line and gray shading represent the literature value with corresponding uncertainty,[76] respectively. (b) shows the amount of correction when taking diffusion into account.

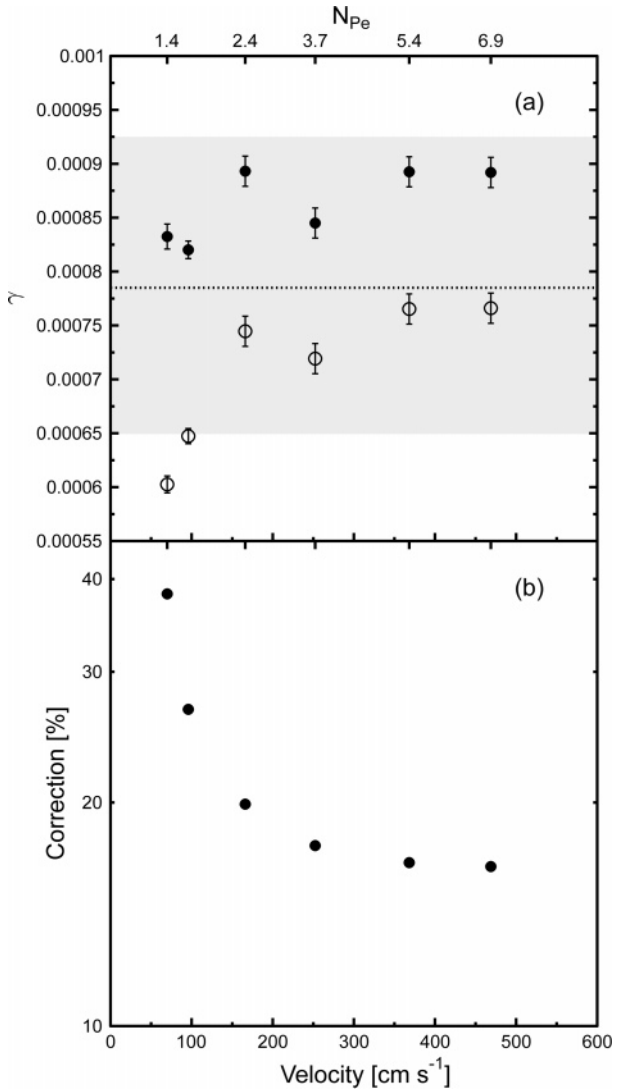

Figure 7. Uptake of O_3 by canola oil as a function of flow velocity and Peclet number (a). Open circles and solid circles indicate γ values that are not corrected for diffusion and are corrected for vertical diffusion and diffusion in the direction of bulk flow, respectively. The dashed line and gray shading represent the literature value with corresponding uncertainty,[76] respectively. (b) shows the amount of correction due to vertical diffusion and diffusion in direction of bulk flow.

60 wt % solutions, and the results from these measurements are reported in Table 3. The uncorrected values (determined using k_{obs} in eq 3) do not agree with literature values. The error in the uncorrected values represents $\pm 1\sigma$. However, after correcting for diffusion using the procedure outlined above and discussed in the Appendix the corrected values are in agreement with the literature data. The uncertainties in the corrected values are mainly due to a 20% uncertainty in the diffusion coefficients.[77]

The general conclusion from the O_3 and N_2O_5 experiments discussed above is that the flow reactor and method of data analysis work well for both slow reactions where γ is approximately 8×10^{-4} and for fast reactions where γ is approximately 0.1

N_2O_5 Reactive Uptake Measurements on Sulfuric Acid Solution Coated with an Organic Monolayer. The reactive uptake of N_2O_5 by an aqueous 80 wt % H_2SO_4 surface coated with an organic monolayer of 1-octadecanol was studied. As mentioned above, these experiments were carried out with a monolayer in contact with a few crystals of 1-octadecanol on the surface. In a separate set of experiments (using a commercial surface pressure sensor with a platinum plate and a commercial Langmuir film balance) we determined the surface pressure and the packing density of the organic monolayer. Using the surface pressure sensor with a platinum plate, we determined that the surface pressure is 36 ± 1 mN m^{-1}. Using the Langmuir film balance and a standard procedure,[55] we measured the pressure−area isotherm for the organic monolayer on the aqueous solution, and then from this information, we were able to conclude that the packing density of the organic monolayer is 22.5 Å^2 molecule^{-1}.

After determining the properties of the monolayer, we then measured the reactive uptake coefficient. The obtained reactive uptake coefficient of N_2O_5 by aqueous 80 wt % H_2SO_4 coated by octadecanol is $(8.1 \pm 3.2) \times 10^{-4}$. This number is based on eight uptake experiments for three individually prepared organic films. We did not observe any time dependence of the reactive uptake coefficient during the course of these experiments. This value is about 2 orders of magnitude lower compared to the reactive uptake on pure aqueous 80 wt % H_2SO_4 solutions. In Table 4 we compare our measures of N_2O_5 uptake with previous

TABLE 3: Experimentally Obtained Reactive Uptake Coefficients for the Uptake of N_2O_5 by Aqueous 60 and 80 wt % H_2SO_4 Solutions and N_2O_5 by Aqueous 80 wt % H_2SO_4 Solutions Coated with a Monolayer of Octadecanol[a]

solution	uncorr γ	corr γ	% correction	literature[b]
60 ± 1 wt % H_2SO_4/H_2O[c]	$(1.6 \pm 0.4) \times 10^{-2}$	$(4.9^{+5.5}_{-1.1}) \times 10^{-2}$	306	3.2×10^{-2} to 8.5×10^{-2}
80 ± 1 wt % H_2SO_4/H_2O[d]	$(1.9 \pm 0.4) \times 10^{-2}$	$(5.0^{+1.9}_{-0.5}) \times 10^{-2}$	263	4.2×10^{-2} to 10.8×10^{-2}
$C_{18}H_{37}OH$ + 80 ±1 wt % H_2SO_4/H_2O[e]	$(7.4 \pm 2.6) \times 10^{-4}$	$(8.1 \pm 3.2) \times 10^{-4}$	21	

[a] Uncorrected γ values do not consider diffusion of the gas-phase species. The error represents $\pm 1\sigma$. Corrected γ values are corrected for vertical diffusion and diffusion in direction of bulk flow. The corresponding error is due to an assumed 20% error in the diffusion coefficients.[77] The amount of correction due to consideration of vertical diffusion and diffusion in direction of bulk flow is given as percentage. In addition, the literature value for the uptake of N_2O_5 by aqueous H_2SO_4 solutions is given for comparison. [b] Mozurkewich and Calvert,[78] Hanson and Ravishankara,[82] Fried et al.,[41] Hu and Abbat,[42] Robinson et al.,[43] Hallquist et al.,[44] Kane et al.[45] [c] Measured at (273 ± 1) K. [d] Measured at (295 ± 0.5) K. [e] Measured at (298 ± 0.5) K.

TABLE 4: Comparison of Measured Reactive Uptake Coefficients of N_2O_5 by Aqueous H_2SO_4 and NaCl Solutions Coated with Organic Monolayers of Different Chain Lengths[a]

literature	monolayer	subphase	temp, K	γ	chain length	factor decrease in γ
this study	octadecanol	H_2SO_4/H_2O	298	$(8.1 \pm 3.2) \times 10^{-4}$	18	62
McNeill et al.[35]	sodium dodecyl sulfate	$NaCl/H_2O$	295	$(2 \pm 1) \times 10^{-3}$	12	10
Thornton and Abbatt[32]	hexanoic acid	$NaCl/H_2O$	295	$(8 \pm 4) \times 10^{-3}$	6	3.5
Park et al.[38]	hexanol	H_2SO_4/H_2O	216	$(6 \pm 1) \times 10^{-2}$	6	2.5
Park et al.[38]	butanol	H_2SO_4/H_2O	216	$(1 \pm 0.2) \times 10^{-1}$	4	1.5

[a] The factor decrease of the reactive uptake coefficient due to an organic monolayer coating compared to the corresponding bare aqueous solution is given.

measurements that also studied the uptake of N_2O_5 in the presence of monolayers. The previous work has focused on organic monolayers of sodium dodecyl sulfate, hexanoic acid, hexanol, and butanol.[32,35,38] In these studies the decrease in γ in the presence of the organic monolayer ranged from 1 to 10. In our case we observed a larger decrease, which is likely in part related to the chain length. In the future we will systematically study the effect of monolayer properties such as chain length, surface pressure, and packing density.

Atmospheric Implications

N_2O_5 heterogeneous reactions on aqueous particles are known to be an important sink of NO_x in the atmosphere.[3,12] Reactions of N_2O_5 on aqueous solutions have been studied extensively, and more recently researchers have begun to investigate the effect of organic monolayers on this chemistry (see Table 4 and the discussion above). This recent research has focused on mainly short chained and soluble monolayers, and in these studies a decrease in the reactive uptake coefficient of between 1 and 10 was observed. In our studies with long chained and insoluble organic monolayers (C18) we observed a decrease of a factor of approximately 62. Evans and Jacob[12] show that a decrease by a factor of 5 compared to the previous study of Dentener and Crutzen[3] can change predictions of NO_x, O_3, and OH concentrations by 7%, 4%, and 8%, respectively. A decrease in the reactive uptake by 2 orders of magnitude would drastically change the atmospheric composition. However, our results should be considered as a lower limit to γ, because monolayers in the atmosphere will likely also contain organic molecules of shorter chain length and also branched organic molecules, which will most likely have a smaller effect on γ. Further studies using the flow reactor presented here will address this point by using more atmospherically relevant monolayers.

Conclusions

A new flow reactor has been developed that allows the study of heterogeneous kinetics occurring on a planar aqueous surface. Here, the effect of an organic monolayer of 1-octadecanol ($C_{18}H_{37}OH$) on the heterogeneous kinetics of N_2O_5 and aqueous H_2SO_4 surfaces has been studied. Computational fluid dynamics simulations have been applied in the development of the flow dynamics for various experimental conditions. These results were used to set up a novel mathematical framework to derive the true first-order wall loss rate coefficient, k_w^{1st}, from the experimentally observed wall loss rate, k_{obs}, under consideration of vertical diffusion and diffusion in flow direction of the gas-phase reactant. The results indicate that neglecting diffusion can lead to measured reactive uptake coefficients that are erroneous by several 100%. Validation of the new apparatus has been performed by measuring the uptake of O_3 by canola oil as a function of pressure and flow velocity. Additional validation has been performed by measuring the reactive uptake coefficients of N_2O_5 by aqueous 60 wt % and 80 wt % H_2SO_4 solutions.

The reactive uptake of N_2O_5 by aqueous H_2SO_4 surfaces coated with an organic monolayer of 1-octadecanol has been measured. The packing density of the 1-octadecanol monolayer in the uptake experiments was 22.5 Å^2 molecule^{-1}, indicating a monolayer in a condensed state. The measured reactive uptake coefficient was determined to be $(8.1 \pm 3.2) \times 10^{-4}$. This is almost 2 orders of magnitude lower than the uptake by the bare aqueous H_2SO_4 solution.[41−45,78,79] The data indicate that the uptake may partly depend on the monolayer chain length based on a comparison of our results with previous literature values.[32,35,38] The reactive uptake coefficient on coated aqueous H_2SO_4 surfaces obtained here may serve as a lower limit for atmospheric aerosols because monolayers in the atmosphere, most likely, also contain organic molecules of different chain lengths, and branched structures which will have a smaller effect on the reactive uptake kinetics.

Appendix

Mathematical Procedure To Derive k_w^{1st} from k_{obs}. To determine k_w^{1st} from k_{obs}, we have developed a mathematical procedure to predict the concentration profile of the reactive species in our rectangular channel flow reactor for an assumed

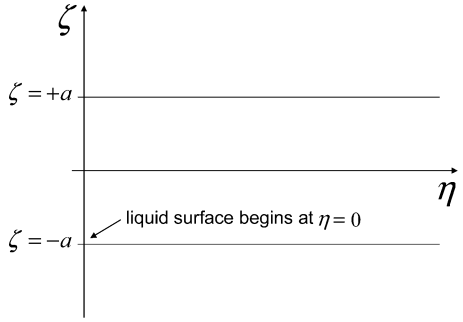

Figure 8. Geometry of the physical problem in general coordinates that is applied to solve numerically the uptake of a gas species by a liquid surface. The cover of the flow reactor is located at $+a$, and the reactive surface is located at $-a$. Adapted from Gidaspow and Solbrig.[67]

k_w^{1st}. The numerical solution considers reaction at the liquid surface, diffusion to the liquid surface (i.e., diffusion in the *y*-direction), and diffusion along the length of the reactor (*x*-direction). We first assume a k_w^{1st} value and use the mathematical procedure to predict concentrations as a function of reaction distance. Then we plot the natural logarithm of the calculated concentration versus the reaction time to determine a calculated first-order rate, k_{obs}^{calc}. When determining k_{obs}^{calc}, we do not include the concentrations in the first 2 cm, because over this region the reactants are establishing a steady-state profile. We then adjust k_w^{1st} in the above calculation until k_{obs}^{calc} is in agreement with k_{obs} (obtained from plots similar to Figure 5). Below we outline the method of predicting concentrations as a function of reaction distance.

The starting point for calculating the concentration profiles in our flow reactor is the continuity equation, which describes convection, reaction at the aqueous solution, and diffusion. To simplify the calculations, we treat our system as a parallel plate flow reactor with one reactive surface. This is the same approach used by Solbrig and Gidaspow[61,67] to analyze the results from their experiments, which also involved a rectangular channel flow reactor with one reactive wall or surface and a similar aspect ratio.

Figure 8 indicates the mathematical problem in general coordinates. It is assumed that the heterogeneous reaction begins at $\eta = 0$, the temperature is constant, and changes in the total number of moles of the gas due to reaction are small, so that the laminar profile is preserved. Assuming steady state of the gas-phase reactant concentration *C* and using Fick's law of diffusion, the following mass balance can be derived

$$v_\eta \frac{\partial C}{\partial \eta} = D\left(\frac{\partial^2 C}{\partial \eta^2} + \frac{\partial^2 C}{\partial \zeta^2}\right) \tag{5}$$

where *C* is the gas-phase reactant concentration and *D* is the diffusion coefficient of the reactant in the carrier gas given in units $cm^2\ s^{-1}$. The general coordinates η and ζ are given in Figure 8. The first two terms on the right-hand side of eq 5 account for diffusion in direction of the bulk flow and for vertical diffusion of the gas-phase reactant. v_η represents the velocity vector in direction of the flow for a parabolic profile and is defined as

$$v_\eta = \frac{3}{2} v_{avg}\left[1 - \left(\frac{\zeta}{a}\right)^2\right] \tag{6}$$

Equation 5 can be rewritten in dimensionless coordinates using eq 6 and the following coordinate transformation[67]

$$x = \frac{\eta}{\frac{3}{2}\frac{v_{avg}a^2}{D}} \quad \text{and} \quad y = \frac{\zeta}{a} \quad \text{and} \quad N_{Pe} = \frac{4a v_{avg}}{D} \tag{7}$$

as

$$(1 - y^2)\frac{\partial C}{\partial x} = \frac{1}{\left(\frac{3}{8}N_{Pe}\right)^2}\frac{\partial^2 C}{\partial x^2} + \frac{\partial^2 C}{\partial y^2} \tag{8}$$

where *x* and *y* are the dimensionless coordinates substituted from eq 7. N_{Pe} represents the Peclet number, which can be interpreted as the ratio between system length and diffusion length. The dimensionless formal physical problem to solve is eq 8 and the following boundary conditions

$$C(0,y) = 1 \tag{9}$$

$$\frac{\partial C}{\partial y}(x,a) = 0 \tag{10}$$

$$\frac{\partial C}{\partial x}(x_{end},y) = 0 \tag{11}$$

$$\frac{\partial C}{\partial y}(x,-a) = -K_w C(x,-a) \tag{12}$$

where

$$K_w \equiv \frac{k_w a}{D} \tag{13}$$

$$k_w^{1st} = \frac{k_w}{h} \tag{14}$$

x_{end} indicates the end of the reactive surface and gives the total length of the reactive surface. K_w is the true dimensionless first-order reaction rate. k_w is the true first-order wall loss rate in units $cm\ s^{-1}$. Equation 9 states that at the beginning of the reactive surface the normalized gas-phase reactant concentration is 1. Equation 10 indicates that no changes in the gas-phase reactant concentration occur at the cover of the flow reactor. Equation 11 indicates that no changes in the gas-phase reactant concentration occur beyond the reactive surface. Equation 12 describes a first-order loss at the liquid surface.

The differential equation and corresponding boundary conditions cannot be solved analytically without further assumptions (see, e.g., discussion in Solbrig[80]), and for this reason a finite differences scheme is employed to solve this problem numerically. The applied computational grid is shown in Figure 9. The size of the computational grid is given by the number of subdivisions with size Δx along the length and with size Δy along the height of the flow reactor. Equation 8 and the boundary conditions eqs 9−12 are solved using second-order approximations for the derivatives. The numerical solution including the setup of the corresponding matrix equation is described below. From this the concentration $C_{i,j}$ at each point *i*, *j* of the computational grid shown in Figure 9 is obtained.

The differential equation and corresponding boundary conditions (eqs 8−12) are discretized for a finite differences scheme

as shown in Figure 9. The differential equation (eq 8) is solved using centered second-order approximations of the derivatives:

$$\frac{\partial C}{\partial y} = \frac{C_{i-1,j} - C_{i+1,j}}{2\Delta y} \tag{15}$$

$$\frac{\partial^2 C}{\partial y^2} = \frac{C_{i-1,j} - 2C_{i,j} + C_{i+1,j}}{\Delta y^2} \tag{16}$$

$$\frac{\partial C}{\partial x} = \frac{C_{i,j-1} - C_{i,j+1}}{2\Delta x} \tag{17}$$

$$\frac{\partial^2 C}{\partial x^2} = \frac{C_{i,j-1} - 2C_{i,j} + C_{i,j-1}}{\Delta x^2} \tag{18}$$

Using eqs 10−18 and eq 8 yields after grouping for coefficients of $C_{i,j}$

$$\underbrace{\left[\frac{(1-y)^2}{2\Delta x} - \frac{\frac{1}{\left(\frac{3}{8}N_{Pe}\right)^2}}{\Delta x^2}\right]}_{\beta} C_{i,j+1} + \underbrace{\left[-\frac{(1-y)^2}{2\Delta x} - \frac{\frac{1}{\left(\frac{3}{8}N_{Pe}\right)^2}}{\Delta x^2}\right]}_{\beta^*} C_{i,j-1}$$

$$+ \underbrace{\left[\frac{\frac{2}{\left(\frac{3}{8}N_{Pe}\right)^2}}{\Delta x^2} + \frac{2}{\Delta y^2}\right]}_{\theta} C_{i,j} + \underbrace{\left[-\frac{1}{\Delta y^2}\right]}_{\delta} C_{i+1,j} + \underbrace{\left[-\frac{1}{\Delta y^2}\right]}_{\delta} C_{i-1,j} = 0\,. \tag{19}$$

The boundary conditions given by eqs 9−12 are discretized using forward and backward second-order approximations of the derivatives:

$$C(0,y) = 1 \quad \text{results in} \quad C_{i,j=1} = 1 \tag{20}$$

$$\left.\frac{\partial C}{\partial x}\right|_{x=x_{end}} = 0 = \frac{3C_{i,j} - 4C_{i,j-1} + C_{i,j-2}}{2\Delta x}$$

$$\text{results in} \quad C_{i,j} = \frac{4}{3}C_{i,j-1} - \frac{1}{3}C_{i,j-2} \tag{21}$$

$$\left.\frac{\partial C}{\partial y}\right|_{y=a} = 0 = \frac{-C_{i+2,j} + 4C_{i+1,j} - 3C_{i,j}}{2\Delta y}$$

$$\text{results in} \quad C_{i,j} = \frac{4}{3}C_{i+1,j} - \frac{1}{3}C_{i+2,j} \tag{22}$$

$$\left.\frac{\partial C}{\partial y}\right|_{y=-a} = -K_w C$$

$$\frac{3C_{i,j} - 4C_{i-1,j} + C_{i-2,j}}{2\Delta y} = -K_w C_{i,j}$$

$$\text{results in} \quad C_{i,j} = (4C_{i-1,j} - C_{i-2,j})\underbrace{\frac{1}{3 + 2\Delta y K_w}}_{\xi}\,. \tag{23}$$

The resulting algebraic equations are solved by

$$\mathbf{M}C_{i,j} = \vec{S} \tag{24}$$

where **M** represents a matrix and $\vec{S}$ represents a vector. $C_{i,j}$ are the concentrations of the gas-phase reactant at the respective node points shown in the computational grid in Figure 9 expressed in vector format. Equation 24 describes the formal physical problem given by eqs 8−12, however, expressed using eqs 19−23. Equation 24 is solved for $C_{i,j}$ by matrix inversion and subsequent diagonalization.

This matrix equation describes the complete formal problem of the first-order uptake of a gas species by a reactive surface on the bottom of a flow reactor involving vertical diffusion and diffusion in direction of the bulk flow. Equation 24 is solved using the commercial software package Matlab.[81]

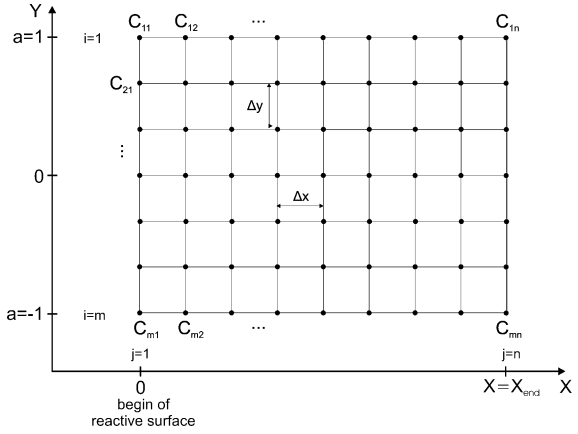

Figure 9. Finite differences grid that is applied to numerically solve the differential equation describing a first-order uptake of a gas species by a liquid surface in our flow reactor. Black points indicate the nodes at which the concentrations of the gas-phase reactant ($C_{i,j}$) are calculated.

Most of the computations were performed using the dimensionless subdivisions of $\Delta x = \Delta y = 0.1$. For the experiments analyzed here, this mesh size was fine enough for correct convergence. Decreasing Δx and Δy to 0.05 and 0.025, i.e., increasing the mesh by a factor of 4 and 16, changed the results by less than approximately 3% and 4%, respectively. This illustrates that the calculations are approaching a limit. Four percent is considered small when considering typical experimental uncertainties in reactive uptake experiments.

To test our mathematical procedure, we compared our calculations with calculations by Solbrig and Gidaspow.[67] These authors also calculated concentration profiles in a parallel plate flow reactor with one catalytic wall, but only considered diffusion in the direction perpendicular to the reactive surface or catalytic wall (i.e., diffusion in the vertical direction). We have carried out calculations of concentration profiles using our mathematical procedure and the same conditions (N_{Pe}, x, K_w) as used by Solbrig and Gidaspow.[67] Our predictions of concentrations as a function of reaction length are within 3% of the concentrations predicted by Solbrig when the Peclet number was greater than 100. When $N_{Pe} > 100$ diffusion in the direction of the bulk flow is not important, and our calculations should agree with the predictions of Solbrig and Gidaspow.[67] The good agreement between the two mathematical solutions at high Peclet numbers gives us additional confidence in our numerical procedure.

As discussed above, to simplify the calculations, we treat our system as a parallel plate flow reactor with one reactive surface. In other words, we calculate the concentration profiles for a parallel plate flow reactor, rather than a rectangular flow reactor. Solbrig and Gidaspow[61] showed that calculations for a parallel plate flow reactor can be applied directly to a rectangular flow reactor, if a reduced dimensionless length, x^*, is used rather than the actual length, when making the comparison. The reduced dimensionless length is given as

$$x^* = \frac{\eta}{\frac{3}{2}\frac{(1+\epsilon)\nu_{avg}a^2}{D}} \tag{25}$$

where $\epsilon = h \cdot \text{width}^{-1}$ is the aspect ratio of the rectangular channel. Hence, when comparing our predictions of concentration profiles discussed above with our experimental measure-

ments, we always compare concentrations as a function of x^* rather than the concentrations as a function of the actual length. In our calculations, k_w^{1st} is adjusted until a good agreement is obtained between the calculations and measurements of concentrations as a function of x^*. Using x^* rather than the actual length, i.e., accounting for rectangular geometry, results in an additional correction of k_w^{1st}. The typical correction for slow reactive uptake coefficients ($\gamma \approx 1 \times 10^{-3}$) is approximately 15%, and for fast uptake coefficients ($\gamma \approx 0.01$), the correction is approximately 50%.

Nomenclature

η = general coordinate
ζ = general coordinate
x = dimensionless coordinate, $\eta/[^3/_2(\upsilon_{avg}a^2/D)]$
x_{end} = length of reactive surface in dimensionless coordinates
x^* = reduced dimensionless coordinate,[61] $\eta/\{^3/_2[(1+\epsilon)\upsilon_{avg}a^2/D]\}$
y = dimensionless coordinate, ζ/a
h = height of flow reactor
$a = h/2$
width = width of channel
ϵ = aspect ratio of channel, h/width
υ_{avg} = average flow velocity
C = concentration of gas-phase reactant species
υ_η = flow velocity vector in η direction
p = partial pressure of gas species in flow reactor
Re = Reynolds number
N_{Pe} = Peclet number, $4a\upsilon_{avg}/D$
l_e = entrance length to establish laminar flow profile, $\approx 0.1 \cdot a \cdot Re$
D = diffusion coefficient of gas-phase reactant in carrier gas
K_w = dimensionless first-order wall rate constant
k_w = first-order wall reaction rate constant in cm s^{-1}
k_{obs} = experimentally observed first-order wall rate constant in s^{-1}
k_{obs}^{cal} = calculated observed first-order wall rate constant in s^{-1}
k_w^{1st} = first-order wall rate constant in s^{-1}
γ = reactive uptake coefficient, $(4k_w^{1st}V/(cA + 2k_w^{1st}V)$
c = thermal molecular speed of gas-phase reactant
A = reactive surface area, $x_{end} \cdot$width
V = volume above reactive surface, $x_{end} \cdot h \cdot$width
$C_{i,j}$ = concentration of gas-phase reactant at position i,j in computational grid
m = number of nodes in y direction in computational grid
n = number of nodes in x direction in computational grid
β = coefficient in finite differences scheme
β^* = coefficient in finite differences scheme
θ = coefficient in finite differences scheme
δ = coefficient in finite differences scheme
ξ = coefficient in finite differences scheme
$\mathbf{M}$ = matrix representing the algebraic equations
$\vec{S}$ = vector for algebraic equations

Acknowledgment. A. Pant and S. Rogak are acknowledged for helpful comments on the development of the flow reactor. This work was funded by the Natural Science and Engineering Research Council of Canada, NSERC, and the Canada Foundation for Innovation, CFI.

References and Notes

(1) Solomon, S.; Garcia, R. R.; Rowland, F. S.; Wuebbles, D. J. *Nature* **1986**, *321*, 755−758.
(2) Molina, M. J.; Tso, T. L.; Molina, L. T.; Wang, F. C. Y. *Science* **1987**, *238*, 1253−1257.
(3) Dentener, F. J.; Crutzen, P. J. *J. Geophys. Res.* **1993**, *98*, 7149−7163.
(4) Dentener, F. J.; Carmichael, G. R.; Zhang, Y.; Lelieveld, J.; Crutzen, P. J. *J. Geophys. Res.* **1996**, *101*, 22869−22889.
(5) Ravishankara, A. R.; Rudich, Y.; Talukdar, R.; Barone, S. B. *Philos. Trans. R. Soc. Lond. Ser. B-Biol. Sci.* **1997**, *352*, 171−181.
(6) Gard, E. E.; Kleeman, M. J.; Gross, D. S.; Hughes, L. S.; Allen, J. O.; Morrical, B. D.; Fergenson, D. P.; Dienes, T.; Galli, M. E.; Johnson, R. J.; Cass, G. R.; Prather, K. A. *Science* **1998**, *279*, 1184−1187.
(7) Zhang, Y.; Carmichael, G. R. *J. Appl. Meteorol.* **1999**, *38*, 353−366.
(8) Song, C. H.; Carmichael, G. R. *J. Atmos. Chem.* **2001**, *40*, 1−22.
(9) Ammann, M.; Pöschl, U.; Rudich, Y. *Phys. Chem. Chem. Phys.* **2003**, *5*, 351−356.
(10) Rudich, Y. *Chem. Rev.* **2003**, *103*, 5097−5124.
(11) Pöschl, U. *Angew. Chem.-Int. Ed.* **2005**, *44*, 7520−7540.
(12) Evans, M. J.; Jacob, D. J. *Geophys. Res. Lett.* **2005**, *32*, 10004−10012.
(13) Rudich, Y.; Donahue, N. M.; Mentel, T. F. *Annu. Rev. Phys. Chem.* **2007**, *58*, 321−352.
(14) Heintzenberg, J. *Tellus* **1989**, *41B*, 149−160.
(15) Kanakidou, M. et al. *Atmos. Chem. Phys.* **2005**, *5*, 1053−1123.
(16) Barger, W. R.; Garrett, W. D. *Pure Appl. Geophys.* **1976**, *81*, 3151−3157.
(17) Garrett, W. D. *Pure Appl. Geophys.* **1978**, *116*, 316−334.
(18) Decesari, S.; Facchini, M. C.; Mircea, M.; Cavalli, F.; Fuzzi, S. *J. Geophys. Res.* **2003**, *108*, 4685.
(19) Duce, R. A.; Mohnen, V. A.; Zimmerman, P. R.; Grosjean, D.; Cautreels, W.; Chatfield, R.; Jaenicke, R.; Ogren, J. A.; Pellizzari, E. D.; Wallace, G. T. *Rev. Geophys.* **1983**, *21*, 921−952.
(20) Facchini, M. C.; Decesari, S.; Mircea, M.; Fuzzi, S.; Loglio, G. *Atmos. Environ.* **2000**, *34*, 4853−4857.
(21) Facchini, M. C.; Mircea, M.; Fuzzi, S.; Charlson, R. J. *Nature* **1999**, *401*, 257−259.
(22) Gill, P. S.; Graedel, T. E.; Weschler, C. J. *Rev. Geophys.* **1983**, *21*, 903−920.
(23) Mochida, M.; Kitamori, Y.; Kawamura, K.; Nojiri, Y.; Suzuki, K. *J. Geophys. Res.* **2002**, *107*, art. no.−4325.
(24) Tervahattu, H.; Hartonen, K.; Kerminen, V. M.; Kupiainen, K.; Aarnio, P.; Koskentalo, T.; Tuck, A. F.; Vaida, V. *J. Geophys. Res.* **2002**, *107*, 4053.
(25) Tervahattu, H.; Juhanoja, J.; Kupiainen, K. *J. Geophys. Res.* **2002**, *107*, 4319.
(26) Tervahattu, H.; Juhanoja, J.; Vaida, V.; Tuck, A. F.; Niemi, J. V.; Kupiainen, K.; Kulmala, M.; Vehkamäki, H. *J. Geophys. Res.* **2005**, *110*, D06207.
(27) Donaldson, D. J.; Vaida, V. *Chem. Rev.* **2006**, *106*, 1445−1461.
(28) Rubel, G. O.; Gentry, J. W. *J. Phys. Chem.* **1984**, *88*, 3142−3148.
(29) Rubel, G. O.; Gentry, J. W. *J. Aerosol. Sci.* **1985**, *16*, 571−574.
(30) Däumer, B.; Niessner, R.; Klockow, D. *J. Aerosol. Sci.* **1992**, *23*, 315−325.
(31) Folkers, M.; Mentel, T. F.; Wahner, A. *Geophys. Res. Lett.* **2003**, *30*, 10004−10012.
(32) Thornton, J. A.; Abbatt, J. P. D. *J. Phys. Chem. A* **2005**, *109*, 10004−10012.
(33) Lawrence, J. R.; Glass, S. V.; Nathanson, G. M. *J. Phys. Chem. A* **2005**, *109*, 7449−7457.
(34) Lawrence, J. R.; Glass, S. V.; Park, S. C.; Nathanson, G. M. *J. Phys. Chem. A* **2005**, *109*, 7458−7465.
(35) McNeill, V. F.; Patterson, J.; Wolfe, G. M.; Thornton, J. A. *Atmos. Chem. Phys.* **2006**, *6*, 1635−1644.
(36) Anttila, T.; Kiendler-Scharr, A.; Tillmann, R.; Mentel, T. F. *J. Phys. Chem. A* **2006**, *110*, 10435−10443.
(37) Gilman, J. B.; Vaida, V. *J. Phys. Chem. A* **2006**, *110*, 7581−7587.
(38) Park, S.-C.; Burden, D. K.; Nathanson, G. M. *J. Phys. Chem. A* **2007**, *111*, 2921−2929.
(39) Clifford, D.; Bartels-Rausch, T.; Donaldson, D. J. *Phys. Chem. Chem. Phys.* **2007**, *9*, 1362−1369.
(40) Hanson, D. R.; Lovejoy, E. R. *Science* **1995**, *267*, 1326−1328.
(41) Fried, A.; Henry, B. E.; Calvert, J. G.; Mozurkewich, M. *J. Geophys. Res.* **1994**, *99*, 3517−3532.
(42) Hu, J. H.; Abbatt, J. P. D. *J. Phys. Chem. A* **1997**, *101*, 871−878.
(43) Robinson, G. N.; Worsnop, D. R.; Jayne, J. T.; Kolb, C. E.; Davidovits, P. *J. Geophys. Res.* **1997**, *102*, 3583−3601.
(44) Hallquist, M.; Stewart, D. J.; Baker, J.; Cox, R. A. *J. Phys. Chem. A* **2000**, *104*, 3984−3990.
(45) Kane, S. M.; Caloz, F.; Leu, M. T. *J. Phys. Chem. A* **2001**, *105*, 6465−6470.
(46) Knopf, D. A.; Anthony, L. M.; Bertram, A. K. *J. Phys. Chem. A* **2005**, *109*, 5579−5589.

(47) Knopf, D. A.; Mak, J.; Gross, S.; Bertram, A. K. *Geophys. Res. Lett.* **2006**, *33*, L17816.
(48) Huey, L. G.; Hanson, D. R.; Howard, C. J. *J. Phys. Chem.* **1995**, *99*, 5001−5008.
(49) Schott, G.; Davidson, N. *J. Am. Chem. Soc.* **1958**, *80*, 1841−1853.
(50) Atkinson, R.; Carter, W. P. L.; Plum, C. N.; Winer, A. M.; Pitts, J. N. *Int. J. Chem. Kinet.* **1984**, *16*, 887−898.
(51) Wayne, R. P.; Barnes, I.; Biggs, P.; Burrows, J. P.; Canosamas, C. E.; Hjorth, J.; Lebras, G.; Moortgat, G. K.; Perner, D.; Poulet, G.; Restelli, G.; Sidebottom, H. *Atmos. Environ. Part A* **1991**, *25*, 1−203.
(52) Carslaw, K. S.; Clegg, S. L.; Brimblecombe, P. *J. Phys. Chem.* **1995**, *99*, 11557−11574.
(53) Massucci, M.; Clegg, S. L.; Brimblecombe, P. *J. Phys. Chem. A* **1999**, *103A*, 4209−4226.
(54) Wexler, A. S.; Clegg, S. L. *J. Geophys. Res.* **2002**, *107*, 4207.
(55) Gaines, G. L. *Insoluble Monolayers at Liquid-Gas Interfaces*; Interscience Publishers: New York, 1966.
(56) Gericke, A.; Simonkutscher, J.; Huhnerfuss, H. *Langmuir* **1993**, *9*, 3115−3121.
(57) Park, S. Y.; Chang, C. H.; Ahn, D. J.; Franses, E. I. *Langmuir* **1993**, *9*, 3640−3648.
(58) Park, S. Y.; Franses, E. *Langmuir* **1995**, *11*, 2187−2194.
(59) Myrick, S. H.; Franses, E. I. *Colloid Surf. A* **1998**, *143*, 503−515.
(60) Fluent Inc. 3d, segregated, laminar, version 6.2.16.
(61) Solbrig, C. W.; Gidaspow, D. *AIChE J.* **1967**, *13*, 346−351.
(62) Levich, V. G. *Physicochemical hydrodynamics*; Prentice Hall: Englewood Cliffs, NJ, 1962.
(63) Brown, R. L. *J. Res. Natl. Bur. Stand. U.S.A.* **1978**, *83*, 1−8.
(64) Motz, H.; Wise, H. *J. Chem. Phys.* **1960**, *32*, 1893−1994.
(65) Hanson, D. R. *J. Phys. Chem. A* **1998**, *102*, 4794−4807.
(66) Walker, R. E. *Phys. Fluids* **1961**, *4*, 1211−1216.
(67) Solbrig, C. W.; Gidaspow, D. *Can. J. Chem. Eng.* **1967**, *45*, 35−39.
(68) Kulacki, F. A.; Gidaspow, D. *Can. J. Chem. Eng.* **1967**, *45*, 72−78.
(69) Mason, E. A.; Monchick, L. *J. Chem. Phys.* **1962**, *36*, 2746−2757.
(70) Monchick, L.; Mason, E. A. *J. Chem. Phys.* **1961**, *35*, 1676−1697.
(71) Fuller, E. N. D. S.; Giddings, J. C. *Indust. Eng. Chem.* **1966**, *58*, 19−27.
(72) Patrick, R.; Golden, D. M. *Int. J. Chem. Kinet.* **1983**, *15*, 1189−1227.
(73) Hanson, D. R.; Burkholder, J. B.; Howard, C. J.; Ravishankara, A. R. *J. Phys. Chem.* **1992**, *96*, 4979−4985.
(74) Moise, T.; Rudich, Y. *J. Geophys. Res.* **2000**, *105*, 14667−14676.
(75) Hanson, D. R.; Ravishankara, A. R. *J. Geophys. Res.* **1991**, *96*, 5081−5090.
(76) de Gouw, J. A.; Lovejoy, E. R. *Geophys. Res. Lett.* **1998**, *25*, 931−934.
(77) Van Doren, J. M.; Barlow, S. E.; Depuy, C. H.; Bierbaum, V. M. *Int. J. Mass Spectrom. Ion Processes* **1991**, *109*, 305−325.
(78) Mozurkewich, M.; Calvert, J. G. *J. Geophys. Res.* **1988**, *93*, 15889−15896.
(79) Hanson, D. R.; Lovejoy, E. R. *Geophys. Res. Lett.* **1994**, *21*, 2401−2404.
(80) Solbrig, C. W. *Chemical Engineering*; Illinois Institute of Technology: Chicago, IL, 1966.
(81) The Mathworks Inc. *Matlab*, release 14.
(82) Hanson, D. R.; Ravishankara, A. R. *J. Phys. Chem.* **1994**, *98*, 5728−5735.